Check for updates

ChemSusChem

Chemistry Europe
European Chemical Societies Publishing
ChemSusChem

RESEARCH ARTICLE OPEN ACCESS

Dual Porphyrin Sensitized Photocatalytic System for Visible-Light-Driven CO_2 Reduction

Anna Katsari[1] | Emmanouil Nikoloudakis[1] | Georgios Charalambidis[2] | Antonios Iliakis[1] | Fabrice Odobel[3] | Emmanuel Stratakis[1,4]

[1]Foundation for Research and Technology (FORTH), Institute of Electronic Structure and Laser (IESL), Heraklion, Greece | [2]Theoretical and Physical Chemistry Institute, National Hellenic Research Foundation, Athens, Greece | [3]Université de Nantes, CNRS, CEISAM UMR 6230, Nantes Cedex, France | [4]Qingdao Innovation and Development Center, Harbin Engineering University, Qingdao, Shandong, P. R. China

Correspondence: Emmanouil Nikoloudakis (enikoloudakis@iesl.forth.gr) | Georgios Charalambidis (gcharal@eie.gr) | Emmanuel Stratakis (stratak@iesl.forth.gr)

Received: 26 June 2026 | **Revised:** 4 September 2026 | **Accepted:** 18 September 2026

Keywords: CO_2 photoreduction | dual sensitization | dye-sensitized photocatalysis | iron porphyrin catalysts | TiO_2 nanoparticles

ABSTRACT

Dye-sensitized photocatalysis offers a powerful strategy for combining the molecular selectivity of transition-metal catalysts with the robustness and charge-separation capabilities of semiconductor materials. Herein, we report a dual porphyrin–sensitized TiO_2 platform for visible-light-driven CO_2 reduction, integrating a Zn-porphyrin photosensitizer with newly designed Fe-porphyrin catalysts bearing urea-based secondary-sphere functionalities. These hydrogen-bonding motifs promote CO_2 preorganization and stabilization of key reduced intermediates at the metal center. Systematic comparison of homogeneous and heterogeneous systems reveals a pronounced enhancement in activity and durability upon immobilization onto TiO_2 nanoparticles. Optimization studies demonstrate that catalytic activity is strongly governed by both sacrificial electron donor (SED) availability and proton concentration. Under anhydrous conditions, increased SED concentration boosts turnover numbers, while the introduction of controlled amounts of water enhances proton-coupled electron transfer but ultimately compromises catalyst stability at higher concentrations. Under optimized conditions, the best-performing assembly achieves turnover numbers (TONs) exceeding 15,000 after 96 h of irradiation, representing, to the best of our knowledge, the highest reported TON for Fe-porphyrin-based dye-sensitized photocatalytic systems (DSPs). These findings highlight the delicate balance between electron and proton management in dye-sensitized architectures and provide key design principles for developing durable and efficient molecular–semiconductor hybrids for solar-driven CO_2 conversion.

1 | Introduction

The rapid rise of atmospheric CO_2 concentrations due to anthropogenic emissions has intensified global efforts to develop sustainable technologies capable of mitigating climate change [1]. Among these, the photocatalytic reduction of CO_2 into value-added fuels and chemicals, such as CO, formic acid, methanol, and hydrocarbons, represents an attractive approach that couples solar energy harvesting with carbon valorization [2, 3]. Achieving efficient CO_2 activation and selective conversion under mild conditions, however, remains a critical challenge due to the chemical inertness of CO_2 and the competitive hydrogen evolution reaction (HER) [4].

Molecular photocatalysts, particularly transition-metal porphyrins, have demonstrated remarkable selectivity for CO formation through well-defined reaction pathways [5–7]. Nevertheless, their practical implementation is often hindered by limited long-term stability, catalyst deactivation, and inefficient charge separation in solution-phase systems [8, 9]. In contrast, heterogeneous

This is an open access article under the terms of the Creative Commons Attribution-NonCommercial License, which permits use, distribution and reproduction in any medium, provided the original work is properly cited and is not used for commercial purposes.

© 2026 The Author(s). *ChemSusChem* published by Wiley-VCH GmbH.

semiconductors such as TiO_2 offer excellent robustness and recyclability but suffer from poor visible light absorption and rapid charge recombination [10–12]. Dye-sensitized photocatalysis has emerged as a promising hybrid strategy that merges the advantages of both approaches, enabling visible-light excitation, efficient charge separation, and spatial organization of catalytic components [13, 14]. In a typical dye-sensitized photocatalytic (DSP) scheme, a photosensitizer (PS) absorbs visible light and injects electrons into the conduction band of TiO_2, from where they migrate to a surface-anchored CO_2-reduction catalyst (CAT). Simultaneously, the oxidized PS is regenerated by a sacrificial electron donor (SED), enabling sustained catalytic turnover [15, 16]. Recent studies have highlighted the importance of secondary-sphere interactions, such as hydrogen bonding and electrostatic stabilization, in enhancing CO_2 binding and suppressing HER pathways in Fe-porphyrin catalysts [17–21]. More particularly, Aukauloo and coworkers reported that iron porphyrins decorated with urea groups act as a multipoint hydrogen-bonding scaffold toward the CO_2 substrate, which importantly boosts the photocatalytic activity [22–24].

Despite significant advances, the rational design of photocatalytic CO_2 reduction systems remains hindered by an incomplete understanding of the factors that limit long-term catalytic turnover, particularly the interplay between charge management, proton availability, and catalyst stability [25]. Separating these coupled effects is essential for developing molecular–semiconductor hybrid systems that combine high activity with sustained durability.

In this work, we address these challenges by developing a dual porphyrin–sensitized TiO_2 system that combines a Zn-porphyrin PS with newly synthesized Fe-porphyrin CATs bearing urea-based hydrogen-bonding functionalities. Through systematic optimization of the catalyst structure, electron-donor concentration, and proton availability, we uncover key performance-limiting factors governing long-term activity and stability. Our results establish design principles for balancing proton-coupled reactivity and catalyst durability, enabling record-high turnover numbers (TONs) in Fe-porphyrin-based heterogeneous DSP systems.

2 | Results and Discussion

The photocatalytic systems investigated in this work are based on a DSP architecture, in which both the molecular CAT and the PS are immobilized onto TiO_2 nanoparticles. As illustrated schematically in Figure 1, the system combines a Zn-porphyrin (**ZnP**) PS with two structurally related iron porphyrin (FeP) catalysts, **CAT(1)** and **CAT(2)**, bearing carboxylate anchoring groups for chemisorption onto TiO_2 and urea-based secondary-sphere functionalities designed to stabilize CO_2-derived intermediates through hydrogen-bonding interactions. Unlike most molecular photocatalytic CO_2 reduction systems reported to date, which predominantly rely on Ru- or Ir-based PSs and Ru- or Re-based catalysts [26–29], the present system is constructed entirely from earth-abundant Zn- and Fe-porphyrins without compromising the catalytic performance.

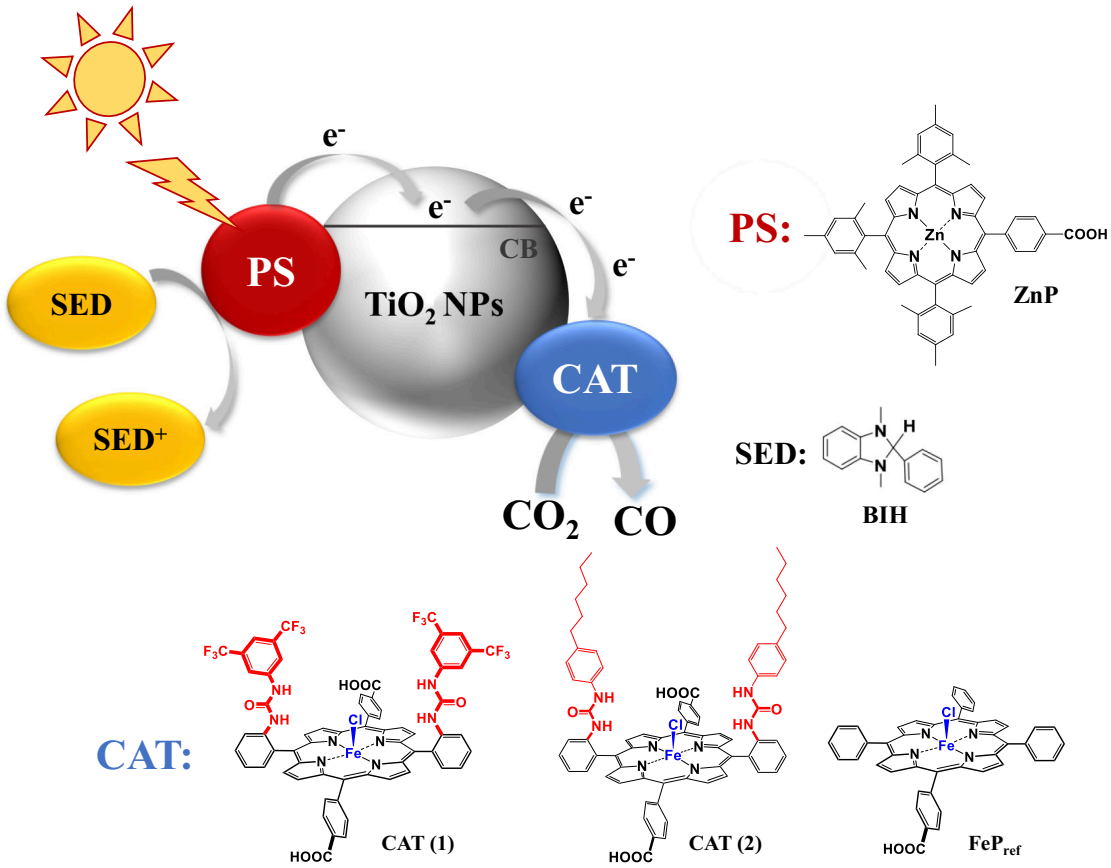


FIGURE 1 | Schematic illustration of the DSP systems investigated herein along with the chemical structures of Fe-porphyrin catalysts, Zn-porphyrin photosensitizer and BIH sacrificial electron donor.

1864564x, 2026, 19, Downloaded from https://chemistry-europe.onlinelibrary.wiley.com/doi/10.1002/cssc.71128 by Cochrane Greece, Wiley Online Library on [13/10/2026]. See the Terms and Conditions (https://onlinelibrary.wiley.com/terms-and-conditions) on Wiley Online Library for rules of use; OA articles are governed by the applicable Creative Commons License

The overall operating principle of this DSP assembly relies on sequential photoinduced electron transfer processes involving the ZnP PS, TiO_2 semiconductor, Fe-porphyrin catalyst, and 1,3-dimethyl-2-phenyl-2,3-dihydro-1H-benzimidazole (BIH) SED. Based on previous studies on zinc porphyrin sensitizers in dye-sensitized solar cells (DSSC) [30–33] and DSPs [26, 34, 35], we can reasonably assume that upon light absorption, ZnP∗ decays by ultrafast electron injection into the TiO_2 conduction band [36, 37]. The radical cation is certainly quickly regenerated by BIH SED, as previously evidenced in previous works [34, 38]. The TiO_2 nanoparticle plays the role of an electron relay to shuttle an electron into the co-loaded FeP catalyst to form the first reduced catalyst, as it usually does in DSPs [39]. The oxidized BIH^+ decomposes into the radical $BIH^{\cdot}$, which is known to be a strong reducer [40]. The latter most likely donates a second electron to FeP in order to generate the active catalytic species. Finally, the doubly reduced FeP activates CO_2 into CO according to the mechanism previously reported for such a type of catalyst [22–24]. Direct photoexcitation of FeP cannot be excluded, but its excited state is known to relax within picoseconds via an internal ligand-to-metal charge-transfer cascade rather than persisting for electron injection into TiO_2 [41], unlike the nanosecond-lived singlet state of ZnP [42]. Moreover, the more positive oxidation potential of FeP [43] versus ZnP [36] makes the former a poor reductant in the excited state. In this scheme, each component fulfills a distinct function: ZnP acts exclusively as the visible-light-active unit for photocatalysis, TiO_2 plays the role of an electron relay and electron reservoir and spatial charge-separation medium preventing direct ZnP–FeP recombination, and FeP is the sole site of CO_2 binding and multi-electron reduction, with its urea arms providing the secondary-sphere hydrogen-bonding environment required to stabilize the CO_2-derived intermediate at the metal center.

2.1 | Synthesis and Characterization

The iron porphyrins **CAT(1)** and **CAT(2)** were successfully synthesized through the pathway outlined in Figures S1 and S2, enabling the incorporation of urea moieties and carboxylate anchoring groups. The synthetic pathway involved the initial preparation of the substituted 5-(4-carbomethoxyphenyl)dipyrromethane (**1**) via an acid-catalyzed condensation of methyl 4-formylbenzoate with an excess of pyrrole under acidic conditions [44–46]. Condensation of dipyrromethane **1** with 2-nitrobenzaldehyde in dichloromethane, catalyzed by TFA and followed by oxidation with DDQ, afforded the *meso*-substituted porphyrin **2**, bearing two nitro groups at the *ortho* positions of the phenyl groups. Subsequent reduction of the nitro functionalities using $SnCl_2$ in an acidic medium led to the corresponding amino-porphyrin **3** [47]. Chromatographic separation allowed the isolation of the two atropisomers, $\alpha\beta$ and $\alpha\alpha$, with the $\alpha\alpha$ atropisomer being selected as the key precursor for the synthesis of the urea-functionalized porphyrins. Reaction of the $\alpha\alpha$-atropisomer of porphyrin **3** with 3,5-bis(trifluoromethyl)phenyl isocyanate at room temperature resulted in the formation of urea linkages at the *ortho*-amino groups, yielding porphyrin **Ur(1)P**. In a parallel synthetic route, the amino groups of porphyrin **3** were first converted into reactive isocyanate intermediates using triphosgene, and subsequent addition of 4-hexylaniline afforded porphyrin **Ur(2)P**, which also incorporates urea functionalities. Metallation of urea-functionalized porphyrins **Ur(1)P** and **Ur(2)P** with iron(II) bromide in dry and deaerated THF in the presence of 2,6-lutidine under an inert atmosphere yielded the corresponding iron(III) porphyrin complexes **Fe–Ur(1)P** and **Fe–Ur(2)P**, respectively. Finally, basic hydrolysis of the methyl ester groups, followed by acidification, led to the deprotected carboxylic acid derivatives **CAT(1)** and **CAT(2)**, which constitute the final iron porphyrin catalysts.

All intermediate compounds were fully characterized by ^1H and ^{13}C nuclear magnetic resonance (NMR) spectroscopy (Figures S3–S13), while the metallation with Fe and the deprotection of the methyl ester group were confirmed through UV–vis absorption spectroscopy and matrix-assisted laser desorption ionization time-of-flight (MALDI-TOF) mass spectrometry. Electrochemical characterization of **CAT(1)** and **CAT(2)** was carried out by cyclic voltammetry (CV) in DMF under an N_2 atmosphere (Figures S14a,b). Both complexes exhibit three quasi-reversible redox processes, which are noted Fe^{III}/Fe^{II}, formal Fe^{II}/Fe^{I}, and Fe^{I}/Fe^{0} redox couples, although it is admitted that the first reduction is metal-centered, while the second and the third one are ligand-based [48]. Notably, all reduction potentials for **CAT(2)** are shifted anodically relative to those of **CAT(1)**, indicating that the reduced states of **CAT(1)** are more destabilized than those of **CAT(2)**. These results suggest that **CAT(2)** can access catalytically relevant reduced intermediates more readily than **CAT(1)**. To further support this point, CV experiments were performed after purging the electrolyte with CO_2 in the presence of 1 M water as a proton source (Figures S14c,d). Under these conditions, both catalysts display an increase in the cathodic current, with an earlier onset of the catalytic wave compared to the corresponding traces recorded under Ar. This confirms that the observed catalytic current is associated with CO_2 reduction rather than proton reduction. Importantly, **CAT(2)** exhibits a less negative catalytic onset potential (−1.35 V vs. Ag/AgCl) than **CAT(1)** (−1.40 V vs. Ag/AgCl), confirming the lower overpotential of **CAT(2)**. In addition, the catalytic current observed for **CAT(2)** is higher than that of **CAT(1)** under the same catalyst concentration, indicating faster catalytic kinetics. The detailed electrocatalytic properties of these catalysts are beyond the scope of the present work and will be the subject of future investigations.

2.2 | Preparation of Dye-Sensitized Photocatalytic Assemblies

Following the synthesis and full characterization of the iron porphyrin catalysts, their immobilization onto TiO_2 nanoparticles was investigated in order to construct the heterogeneous dye-sensitized photocatalytic assemblies. Both **CAT(1)** and **CAT(2)** bear para-carboxylate anchoring groups, which enable their chemisorption onto the TiO_2 surface. Adsorption was carried out by suspending TiO_2 nanoparticles in mixed toluene/ethanol solutions of the respective iron porphyrins. UV–vis absorption spectra recorded before and after adsorption revealed highly efficient adsorption of both catalysts (Figures S15–S18). Quantitative analysis of the filtrates showed nearly complete adsorption at low initial catalyst concentrations and dye-loading efficiencies exceeding 90% in all cases (Table S2), as expected by the strong affinity of the carboxylic acid-functionalized porphyrins for the TiO_2 surface. Subsequent sensitization with the zinc porphyrin photosensitizer (**ZnP**) was performed by exposing the

1864564x, 2026, 19, Downloaded from https://chemistry-europe.onlinelibrary.wiley.com/doi/10.1002/cssc.71128 by Cochrane Greece, Wiley Online Library on [13/10/2026]. See the Terms and Conditions (https://onlinelibrary.wiley.com/terms-and-conditions) on Wiley Online Library for rules of use; OA articles are governed by the applicable Creative Commons License

Fe-porphyrin–TiO_2 composites to **ZnP** solutions in chloroform. Importantly, the presence of the surface-bound iron porphyrin catalyst did not impede **ZnP** adsorption, and high PS loadings were likewise achieved (Table S2). UV–vis analysis of the supernatants confirmed efficient ZnP uptake (Figures S15–S18), demonstrating that the dual-sensitization strategy is compatible with sequential surface functionalization. SEM imaging of bare TiO_2, **CAT(2)–TiO_2**, and **CAT(2)–TiO_2–ZnP** showed comparable nanoparticle morphology and aggregation across all three samples, consistent with molecular-scale surface functionalization lying below the SEM resolution (Figure S19). ATR-IR spectra of the same series (Figure S20) are likewise dominated by the TiO_2 support but provide further support for successful immobilization: the free carboxylic acid C═O stretch of neat **CAT(2)** (1693 cm^{-1}) is absent in both TiO_2-supported samples, consistent with deprotonation of the anchoring carboxylic acid upon chemisorption to the TiO_2 surface [49]. Porphyrin ring vibrations retained in both hybrids (1604, 1512, and 1000 cm^{-1}) [50, 51] confirm the presence of intact, surface-bound **CAT(2)**.

The resulting CAT–TiO_2–ZnP assemblies exhibit well-defined and reproducible surface compositions, with comparable amounts of the catalyst and PS incorporated across all systems (Table S3). This controlled loading is crucial for meaningful comparison of photocatalytic performance, ensuring that differences in activity arise from intrinsic catalyst properties rather than variations in surface coverage.

2.3 | Photocatalytic CO_2 Reduction in Homogeneous and Heterogeneous Systems

To evaluate the effect of anchoring the catalytic components onto TiO_2, homogeneous and heterogeneous CO_2 photoreduction experiments were conducted under identical conditions using **CAT(1)** as a representative catalyst. Figure 2a shows the dependence of CO evolution (expressed as $TON_{(CO)}$) on the concentration of **CAT(1)** in a homogeneous system in the presence of ZnP. Varying the catalyst concentration from 4 to 300 μM leads to a systematic decrease in TON, consistent with competitive light absorption by FeP and possible quenching of the ZnP excited state by the nearby Fe-porphyrins via electron or energy transfer. This competitive, nonproductive absorption of incident light by FeP represents an inherent limitation on the overall light utilization efficiency of the DSP assembly. The optimal concentration was found to be 4 μM, which was subsequently adopted for all DSP experiments. To directly assess the impact of TiO_2 immobilization on the catalytic performance, homogeneous and heterogeneous systems containing identical absolute amounts of catalyst and PS were compared (Figure 2b). The DSP system based on **CAT(1)–TiO_2–ZnP** modestly outperforms its homogeneous analog under short-term, matched-loading conditions (TON = 2708 vs. 2318 after 72 h), while its principal advantage emerges over extended irradiation, where it sustains activity for at least 24 h longer than the homogeneous system (Figure S21, Table 1, entries 1–2). These observations confirm that the TiO_2 nanoparticles effectively mediate charge separation by shuttling electrons from ZnP to the Fe catalyst while spatially segregating oxidized and reduced species, thereby reducing recombination losses and further enable straightforward physical recovery of the photocatalyst from solution by filtration, a practical advantage not accessible for the homogeneous system. The enhanced durability of the DSP assemblies relative to the homogeneous analog is consistent with reports that immobilization of molecular CATs on TiO_2 extends the lifetime of catalytically active reduced intermediates and preserves catalyst integrity during turnover [52]. These advantages should be weighed against known limitations of the heterogeneous format, including competitive light harvesting by co-immobilized species, possible back electron transfer through the TiO_2 conduction band, surface-limited kinetics rather than free solution-phase collision, and light scattering [53] by the TiO_2 particles themselves.

The long-term photocatalytic behavior of the DSP systems was investigated by monitoring the CO evolution as a function of irradiation time. Figure 3a presents the time-dependent CO production using a low catalyst loading (0.016 μmol) for **CAT(1)–TiO_2–ZnP** and **CAT(2)–TiO_2–ZnP** assemblies. Both systems exhibit sustained activity over extended irradiation periods, with **CAT(2)** delivering slightly higher TONs than those of **CAT(1)**. At a higher catalyst loading (0.16 μmol, Figure 3b), the same trend is observed, with **CAT(2)** again

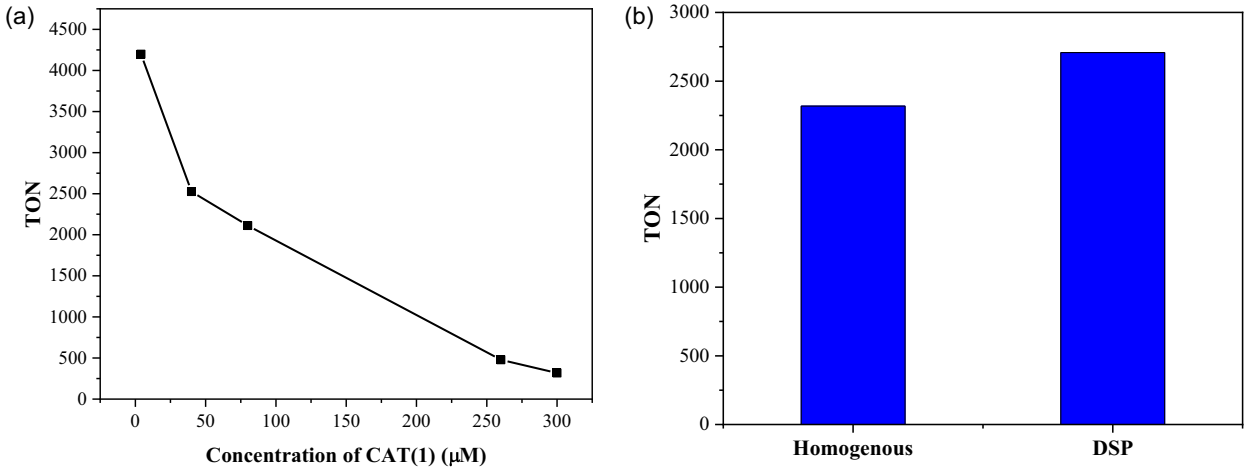


FIGURE 2 | (a) CO evolution (TON_{CO}) in CO_2-saturated ACN solutions containing various concentrations of **CAT(1)**, 70 μM ZnP and 0.1 M BIH after 24 h of irradiation, (b) comparison of CO evolution activity of a homogenous catalytic system and a DSP system both containing 0.16 μmol **CAT(1)**, 0.28 μmol ZnP and 0.1 M BIH after 72 h of irradiation.

1864564x, 2026, 19, Downloaded from https://chemistry-europe.onlinelibrary.wiley.com/doi/10.1002/cssc.71128 by Cochrane Greece, Wiley Online Library on [13/10/2026]. See the Terms and Conditions (https://onlinelibrary.wiley.com/terms-and-conditions) on Wiley Online Library for rules of use; OA articles are governed by the applicable Creative Commons License

TABLE 1 | Summary of photocatalytic CO_2-to-CO reduction performance of all investigated assemblies under different reaction conditions.

	Photocatalyst	CAT, μmol	SED, M	Solvent	CO, μmol	H_2, μmol	Selectivity CO, %	TON_{CO}
1	**CAT(1)–TiO_2–ZnP**	0.16	0.1	ACN	441	2.5	99	2708
2	**CAT(1) + ZnP**	0.16	0.1	ACN	427	2.3	99	2318
3	**CAT(1)–TiO_2–ZnP**	0.016	0.1	ACN	155	21	88	9702
4	**CAT(2)–TiO_2–ZnP**	0.16	0.1	ACN	551	3.5	99	3602
5	**CAT(2)–TiO_2–ZnP**	0.016	0.1	ACN	162	23	88	10 179
6	**CAT(2)–TiO_2–ZnP**	0.16	0.25	ACN	1042	7.5	99	6816
7	**CAT(2)–TiO_2–ZnP**	0.016	0.25	ACN	244	48	83	15 268
8	**CAT(2)–TiO_2–ZnP**	0.016	0.1	ACN/H_2O 1%	178	6.5	96	11 113
9	**CAT(2)–TiO_2–ZnP**	0.016	0.1	ACN/H_2O 3%	255	7	97	15 951
10	**CAT(2)–TiO_2–ZnP**	0.016	0.1	ACN/H_2O 6%	47	3.5	93	2919
11	**CAT(2)–TiO_2–ZnP**	0.016	0.1	ACN/H_2O 10%	ND	3.2	—	—
12	**TiO_2**	—	0.1	**ACN**	ND	ND	—	—
13	**CAT(1)–TiO_2**	0.16	0.1	ACN	ND	ND	—	—
14	**ZnP–TiO_2**	—	0.1	ACN	ND	ND	—	—
15	**CAT(2)–TiO_2–ZnP**	0.16	—	**ACN**	ND	ND	—	—
16	**FeP_{ref}–TiO_2–ZnP**	0.016	0.1	ACN	ND	ND	—	—
17	**FeP_{ref} + ZnP**	0.016	0.1	ACN	**ND**	ND	—	—

Note: Bold values represent the Photocatalyst of each series.

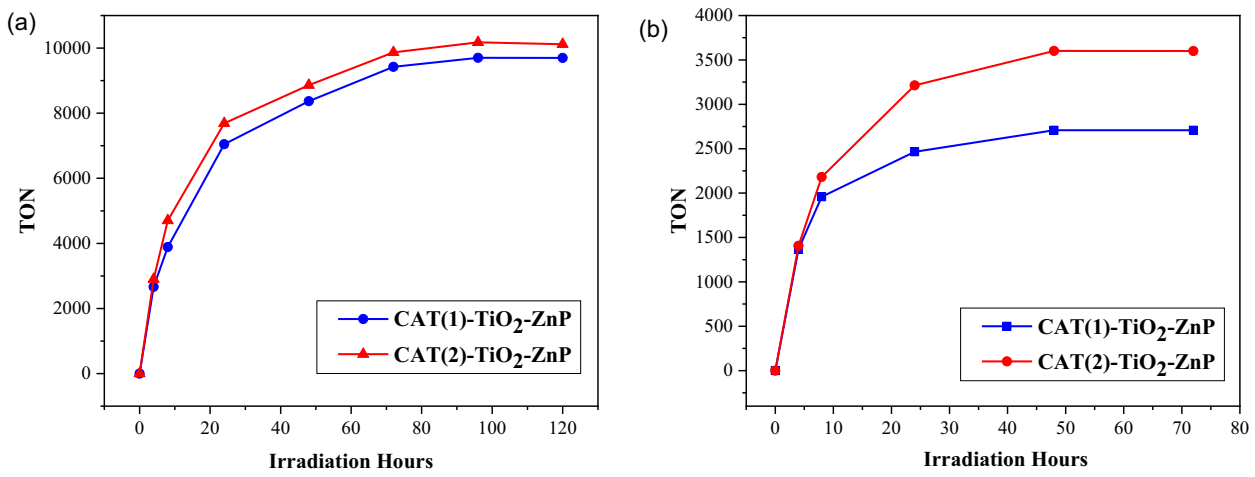


FIGURE 3 | Time-dependent photocatalytic CO_2-to-CO conversion performance of DSP systems consisting of CAT–TiO_2–ZnP assemblies in acetonitrile (4 mL) containing BIH (0.1 M). The ZnP loading was fixed at 0.28 μmol. (a) CO evolution using 0.016 μmol of **CAT(1)** or **CAT(2)**. (b) CO evolution using 0.16 μmol of **CAT(1)** or **CAT(2)**. Blue squares correspond to **CAT(1)–TiO_2–ZnP**, while red triangles correspond to **CAT(2)–TiO_2–ZnP**.

outperforming **CAT(1)** while maintaining prolonged catalytic activity. The comparable activities of **CAT(1)** and **CAT(2)** arise from the presence of urea functionalities in both catalysts, which furnish a similar secondary coordination sphere capable of stabilizing CO_2 and reduced [Fe–CO_2] intermediates [22–24]. The enhanced CO_2 reduction performance of **CAT(2)** could be attributed to lower overpotential and to its stronger binding of CO_2 by the more electron-rich urea arms.

With **CAT(2)** identified as the most effective catalyst, subsequent optimization studies were carried out using this system as a representative platform. We next examined the influence of the SED concentration on the photocatalytic performance of the DSP system under anhydrous conditions (Table 1, entries 4–7). This study was conducted in the absence of added water in order to isolate the effect of electron donor availability and avoid convolution with proton-coupled processes. At a BIH concentration of 0.1 M, CO production gradually reached a plateau, corresponding to TON values of 3602 at higher catalyst loadings, consistent with the near-complete consumption of the sacrificial donor. Increasing the BIH concentration to 0.25 M resulted in a marked extension of catalytic activity and a substantial increase in TON, reaching values up to 6816 under otherwise identical conditions (Figure S22). Notably, under the optimized catalyst concentration

1864564x, 2026, 19, Downloaded from https://chemistry-europe.onlinelibrary.wiley.com/doi/10.1002/cssc.71128 by Cochrane Greece, Wiley Online Library on [13/10/2026]. See the Terms and Conditions (https://onlinelibrary.wiley.com/terms-and-conditions) on Wiley Online Library for rules of use; OA articles are governed by the applicable Creative Commons License

(0.016 μmol of **CAT(2)**), raising the BIH concentration from 0.1 to 0.25 M led to increased $TON_{(CO)}$ values, rising from 10,179 to 15,268 after 96 h of irradiation. These results clearly indicate that, in the absence of added proton sources, the long-term activity of the system is predominantly limited by electron donor availability rather than intrinsic catalyst performance.

Given the crucial role of proton availability in CO_2 reduction, the influence of water concentration on the catalytic performance was systematically examined. As shown in Figure 4a, the addition of controlled amounts of water to the acetonitrile reaction medium leads to a pronounced enhancement in CO production up to an optimal concentration (Table 1, entries 5 and 8–11). This behavior reflects a balance between facilitating proton-coupled electron-transfer steps and suppressing competitive hydrogen evolution. Beyond the optimal water content, a gradual decrease in CO formation is observed, likely due to increased HER activity and partial displacement of surface-bound catalytic species. These results highlight the importance of fine-tuning proton availability in DSP systems to maximize CO_2-to-CO selectivity. Noteworthy, under optimized conditions, the **CAT(2)–TiO_2–ZnP** assembly achieved TON values as high as 15,951 after 96 h of irradiation, representing, to the best of our knowledge, the highest reported TONs for Fe-porphyrin-based heterogeneous DSP systems (Table S4).

To directly probe the durability-limiting step of the DSP assembly, we performed selective replenishment experiments (Figure 4b), an approach consistent with mechanistic strategies used to isolate the origin of catalyst deactivation in other molecular CO_2-photoreduction systems [54]. As illustrated in Figure 4b, when the photocatalytic system reached a plateau in CO production, selective replenishment of individual components was carried out. CO evolution resumed exclusively upon reintroduction of the iron porphyrin catalyst, whereas the addition of ZnP or BIH alone did not restore activity. This observation confirms that catalyst degradation or deactivation is the primary factor limiting long-term performance, while the PS and sacrificial donor remain largely intact under the applied conditions.

Control experiments in which ZnP, the Fe-porphyrin catalyst, or BIH were individually omitted resulted in no detectable CO production (Table 1, entries 12–15). This confirmed that all three components are required and that the observed activity arises from cooperative interactions within the dual-sensitized TiO_2 assembly. In particular, the absence of CO formation in the control lacking ZnP (Table 1, entry 13) indicates that direct photoexcitation of FeP does not contribute productively to catalysis on its own, consistent with the picosecond-scale internal relaxation of its excited state, as discussed above. Replacing **CAT(1)** or **CAT(2)** with a reference Fe-porphyrin [55] bearing a single carboxylic acid anchoring group but lacking secondary-sphere urea functionalities led to no measurable CO formation, both when immobilized on TiO_2 under otherwise identical conditions (Table 1, entry 16) and as a homogeneous catalyst (Table 1, entry **17**). This confirms, within this system, that the urea-based secondary coordination sphere, rather than surface immobilization alone, is required for catalytic activity. This result is consistent with literature reports indicating that conventional Fe-porphyrin catalysts typically require access to the Fe(0) oxidation state to drive CO_2 reduction, which often necessitates the use of strongly reducing Ru- or Ir-based PSs [27, 56, 57]. In the present DSP system, photoexcitation of the noble-metal-free Zn-porphyrin leads to electron injection into TiO_2, distinguishing it from literature systems that employ noble-metal PSs [39]. Subsequently, the injected electrons are transferred to the Fe-porphyrin and reduce the catalytic center. Notably, the incorporation of urea-based secondary-sphere functionalities enables efficient CO_2 reduction from the Fe(I) state [24, 58].

In contrast to the anhydrous system, increasing the BIH concentration in the presence of 3% water does not lead to further enhancement in CO production, suggesting that catalyst stability and proton-driven degradation pathways, rather than electron donor availability, become the dominant limiting factors under these conditions. Importantly, the heterogeneous nature of the DSP system enables facile recovery of the photocatalyst and contributes to the observed enhancement in durability relative to homogeneous systems.

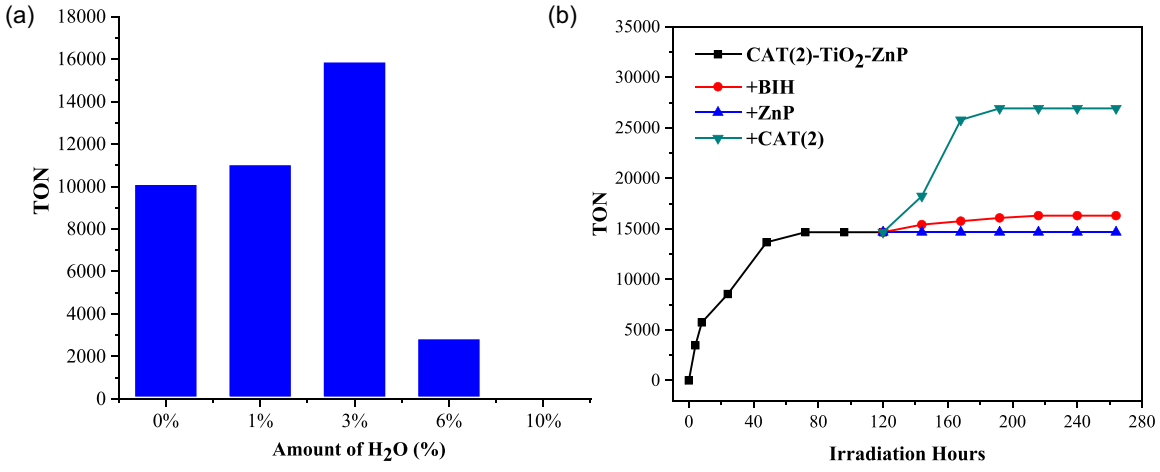


FIGURE 4 | (a) Effect of water concentration on the photocatalytic CO_2-to-CO conversion activity of the DSP system under otherwise identical reaction conditions (0.016 μmol **CAT(2)**, 0.28 μmol ZnP and 0.1 M BIH). (b) Experiment performed after the optimal catalytic system reached a plateau in CO production, in which selected reaction components were sequentially added. CO evolution resumed only upon addition of the catalyst, highlighting its essential role in sustaining photocatalytic activity.

1864564x, 2026, 19, Downloaded from https://chemistry-europe.onlinelibrary.wiley.com/doi/10.1002/cssc.71128 by Cochrane Greece, Wiley Online Library on [13/10/2026]. See the Terms and Conditions (https://onlinelibrary.wiley.com/terms-and-conditions) on Wiley Online Library for rules of use; OA articles are governed by the applicable Creative Commons License

3 | Conclusions

Herein, we developed a dual porphyrin–sensitized TiO_2 photocatalytic platform for visible-light-driven CO_2 reduction, integrating a Zn-porphyrin PS with urea-functionalized Fe-porphyrin catalysts. Immobilization of both components onto TiO_2 nanoparticles offers a modest improvement in short-term catalytic output relative to the homogeneous analog, with its principal benefit residing in extended operational durability, reflecting the advantages of spatial charge separation and catalyst recyclability afforded by the DSP architecture.

Among the catalysts investigated, **CAT(2)** exhibits superior performance, attributable to its electron-donating substituents and secondary-sphere hydrogen-bonding motifs that facilitate CO_2 activation. Systematic optimization studies reveal that catalytic performance is governed by a delicate balance between electron donor availability and proton concentration. Under anhydrous conditions, increasing the BIH concentration effectively alleviates sacrificial donor limitations and enables exceptionally high TONs. In contrast, the introduction of water enhances proton-coupled electron transfer but ultimately accelerates catalyst deactivation at higher concentrations, highlighting proton-induced stability as a critical bottleneck. Under optimized conditions, the **CAT(2)–TiO_2–ZnP** assembly achieves TON values exceeding 15,000 after 96 h of irradiation, representing the highest reported performance for Fe-porphyrin-based heterogeneous DSP systems to date.

We note that the present system balances the benefits of spatial charge separation and catalyst recyclability against the intrinsic limitations of the heterogeneous format, including competitive excitation, back-electron transfer, surface-limited kinetics, and light scattering by the solid support. These findings provide important mechanistic insight into the interplay of electrons, protons, and catalyst stability in dye-sensitized CO_2 reduction and offer clear guidelines for the rational design of next-generation molecular–semiconductor hybrids for solar fuel production.

4 | Experimental Section

4.1 | Materials

All reagents were purchased from common commercial sources and used without any further purification unless otherwise stated.

4.2 | NMR spectroscopy

The porphyrin moieties were analyzed with ^{1}H NMR spectroscopy using Bruker AMX-500 MHz and Bruker DPX-300 MHz spectrometers. All measurements were carried out at room temperature in a deuterated solvent using residual protons as an internal reference.

4.3 | Ultraviolet–Visible (UV–Vis) Absorption Spectroscopy

In all studies, a Shimadzu UV-1700 spectrometer was used. The reported experiments were performed using quartz cuvettes of a 0.2 cm path length.

4.4 | Mass Spectrometry

Mass spectra were obtained on a Bruker UltrafleXtreme MALDI-TOF spectrometer using trans-2-[3-(4-*tert*-butylphenyl)-2-methyl-2-propenylidene] malononitrile (DCTB) as the matrix.

4.5 | Electrochemical Studies

Cyclic and square wave voltammetry experiments were carried out in freshly deoxygenated dimethylformamide (DMF) under a nitrogen atmosphere at room temperature using an AutoLab PGSTAT20 potentiostat. Tetrabutylammonium hexafluorophosphate (n-Bu_4NPF_6, 0.05 M) was employed as the supporting electrolyte. A standard three-electrode configuration was used, consisting of a glassy carbon working electrode, an Ag/AgCl electrode as the reference electrode, and a platinum wire as the counter electrode.

4.6 | Synthesis

4.6.1 | Synthesis of 5-(4-Carbomethoxy-Phenyl) Dipyrromethane [44]

Methyl 4-formylbenzoate (3.00 gr, 18 mmol, 1 equiv.) and pyrrole (3.78 mL, 54 mmol, 3 equiv.) were dissolved in a nitrogen-degassed 0.18 M HCl solution. The mixture was stirred at room temperature for 4 h. After completion of the reaction, the mixture was extracted with CH_2Cl_2. The combined organic layers were dried over anhydrous $MgSO_4$, and the solvent was removed under vacuum. The obtained solid was purified by column chromatography (silica gel, hexane/CH_2Cl_2/EtOAc, 7:2:1 v/v) to give the desired compound as a white solid (1.845 g, 6.58 mmol, 37%). ^{1}H NMR ($CDCl_3$, 500 MHz): δ (ppm) 7.99 (d, J = 8.5 Hz, 2H), 7.95 (bs, 2H), 7.30 (d, J = 8.5 Hz, 2H), 6.73 (m, 2H), 6.17 (m, 2H), 5.90 (s, 2H), 5.53 (s, 1H), 3.91 (s, 3H).

4.6.2 | Synthesis of 5,15-Bis-(2-Nitro-Phenyl)10,20-Bis-(4-Carbomethoxy-Phenyl) Porphyrin

A solution of 5-(4-carbomethoxy-phenyl)dipyrromethene (1.00 g, 3.57 mmol, 1 equiv.) and 2-nitrobenzaldehyde (0.539 g, 3.57 mmol, 1 equiv.) in dichloromethane (400 mL) was degassed by nitrogen bubbling for 15 min, and then trifluoroacetic acid (TFA, 0.55 mL, 7.14 mmol) was added dropwise. The mixture was stirred at room temperature for 30 min, after which 2,3-dichloro-5,6-dicyano-1,4-benzoquinone (DDQ, 1.296 g, 5.71 mmol) was added. The reaction mixture was stirred for an additional 1 h at room temperature and then neutralized with triethylamine (TEA, 1.30 mL). The solvent was evaporated, and the crude product was purified by column chromatography (silica gel, CH_2Cl_2) to afford the mixture of the two atropisomers as a purple solid (0.200 g, 0.244 mmol, 7%). MS (MALDI-TOF): m/z calculated for $C_{48}H_{32}N_6O_8$: 820.23 $[M]^+$ found: 820.45.

4.6.3 | Synthesis of α,α-5,15-Bis(2-Amino-Phenyl)10,20-Bis-(4-Carbomethoxy-Phenyl) Porphyrin

In a 500 mL round-bottom flask, 1 equiv. of 5,15-bis-(2-nitrophenyl)10,20-bis-(4-carbomethoxy-phenyl) porphyrin (0.344 g,

1864564x, 2026, 19, Downloaded from https://chemistry-europe.onlinelibrary.wiley.com/doi/10.1002/cssc.71128 by Cochrane Greece, Wiley Online Library on [13/10/2026]. See the Terms and Conditions (https://onlinelibrary.wiley.com/terms-and-conditions) on Wiley Online Library for rules of use; OA articles are governed by the applicable Creative Commons License

0.413 mmol) was dissolved in 250 mL of CH_2Cl_2. Subsequently, 6.88 mL of concentrated HCl and $SnCl_2$ (1.04 g, 5.45 mmol, 13 equiv.) were added. The reaction mixture was stirred at room temperature for 48 h. After the completion of the reaction, the mixture was neutralized with concentrated aqueous NH_3 (20% w/w). Then, 80 mL of CH_2Cl_2 was added, and the mixture was washed with aqueous $NaHCO_3$ (3 × 100 mL) and brine (3 × 100 mL). The organic layer was dried over anhydrous $MgSO_4$. The resulting mixture of two atropisomers was separated by column chromatography (silica gel and CH_2Cl_2/EtOAc 99:1 to 97:3 v/v). The α,β-isomer was eluted first with CH_2Cl_2/EtOAc (99:1 v/v), followed by the α,α-isomer with CH_2Cl_2/EtOAc (97:3 v/v). In total, 0.250 g (0.329 mmol, 80%) of the product was isolated, comprising 0.135 g (0.177 mmol, 43%) of the α,β-isomer and 0.115 g (0.160 mmol, 39%) of the α,α-isomer. α,α-atropisomer: ^{1}H NMR ($CDCl_3$, 400 MHz): δ (ppm) 8.96 (d, J = 4.4 Hz, 4H), 8.83 (d, J = 4.8 Hz, 4H), 8.47 (d, J = 8.4 Hz, 4H), 8.32 (d, J = 8.4 Hz, 4H), 7.92 (dd, J_1 = 7.2 Hz, J_2 = 1.2 Hz, 2H), 7.66 (td, J_1 = 7.6 Hz, J_2 = 1.2 Hz, 2H), 7.23 (td, J_1 = 7.6 Hz, J_2 = 1.2 Hz, 2H), 7.16 (dd, J_1 = 8 Hz, J_2 = 0.4 Hz, 2H), 4.14 (s, 6H), 3.53 (s, 4H), −2.70 (s, 2H). MS (MALDI-TOF): m/z calculated for $C_{48}H_{36}N_6O_4$: 760.28 $[M]^+$ found: 760.60.

4.6.4 | *Synthesis of Ur(1)P*

3,5-Bis(trifluoromethyl)phenyl isocyanate (99 µL, 0.562 mmol, 6 equiv.) was added to a solution of $\alpha\alpha$-5,15-bis-(2-amino-phenyl)-10,20-bis(4-carbomethoxy-phenyl) porphyrin (0.071 g, 0.094 mmol, 1 equiv.) in dry CH_2Cl_2 (7 mL) under nitrogen. After stirring for 3 h at room temperature, the solvent was removed under vacuum. The expected compound was precipitated by dissolving the crude product in a minimal amount of dichloromethane and adding excess hexane. The solid was collected by filtration, washed with pentane, and dried under vacuum to afford the product as a purple solid (0.080 g, 0.063 mmol, and 67%). ^{1}H NMR (DMSO-d_6, 500 MHz): δ (ppm) 8.82 (d, J = 4.5 Hz, 4H), 8.78 (d, J = 4.5 Hz, 4H), 8.65 (s, 2H), 8.37–8.27 (m, 10H), 8.06 (dd, J_1 = 7.5 Hz, J_2 = 1.5 Hz, 2H), 7.87 (td, J_1 = 7.5 Hz, J_2 = 1.5 Hz, 2H), 7.56 (td, J_1 = 7.5 Hz, J_2 = 1.5 Hz, 2H), 7.43 (s, 4H), 7.37 (s, 2H), 7.30 (s, 2H), 4.01 (s, 6H), −2.80 (s, 2H). ^{13}C NMR (DMSO-d_6, 125 MHz): δ (ppm) 166.8, 152.6, 146.1, 141.5, 139.1, 135.2, 135.0, 132.6, 129.8, 128.3, 124.7, 123.0, 122.7, 122.0, 119.3, 117.4, 115.9, 114.6, 52.9. MS (MALDI-TOF): m/z calculated for $C_{66}H_{42}F_{12}N_8O_6$: 1270.30 $[M]^+$ found: 1270.06.

4.6.5 | *Synthesis of Fe–Ur(1)P*

A solution of Ur(1)P (0.080 g, 0.061 mmol, 1 equiv.) and 2,6-lutidine (140 µL, 1.21 mmol, 20 equiv.) 10 mL of dry THF was degassed by nitrogen bubbling for 15 min. Then, $FeBr_2$ (0.131 g, 0.61 mmol, 10 equiv.) was added, and the reaction mixture was stirred overnight at room temperature under nitrogen. The solvent was evaporated under reduced pressure. The solid was dissolved in 50 mL of CH_2Cl_2 and washed with a 50 mL aqueous solution of 1 M HCl. The organic phase was collected and evaporated under reduced pressure. The crude product was purified by column chromatography (silica gel, CH_2Cl_2 to CH_2Cl_2/MeOH, 98:2 v/v), yielding the iron porphyrin complex as a brown solid (0.070 g, 0.051 mmol, and 84%). MS (MALDI-TOF): m/z calculated for $C_{66}H_{40}F_{12}FeN_8O_6$: 1324.22 $[M–Cl^-]^+$ found: 1323.03.

4.6.6 | *Synthesis of CAT(1)*

In a 100 mL round-bottom flask, 1 equiv. of Fe–Ur(1)P (0.070 g, 0.051 mmol) was dissolved in 78 mL of THF/MeOH in a 2:1 (v/v) ratio. Subsequently, 26 mL of an aqueous 0.36 M KOH solution was added, and the reaction mixture was stirred at room temperature for 48 h. Subsequently, the organic solvents were evaporated under reduced pressure, and distilled water was added to the residue. Acidification of the mixture using an aqueous solution of 1 M HCl resulted in the precipitation of the porphyrin, which was filtered, washed with distilled water, and finally dried under vacuum, yielding the final product as a brown solid (0.065 g, 0.048 mmol, 94%). UV–vis (MeOH) λ_{max} nm (ε, mM^{-1} cm^{-1}) = 340 (31.8), 415 (99.5), 564 (4.5), 607 (3.7), and 650 (2.8). MS (MALDI-TOF): m/z calculated for $C_{64}H_{36}F_{12}FeN_8O_6$: 1296.19, $[M–Cl^-]^+$ found: 1297.68.

4.6.7 | *Synthesis of Ur(2)P*

Under an inert atmosphere, α,α-5,15-bis-(2-amino-phenyl)-10,20-bis(4-carbomethoxy-phenyl) porphyrin (0.050 g, 0.066 mmol, 1 equiv.) was dissolved in dry THF (50 mL) in a 100 mL two-neck round-bottom flask. Triethylamine (73 µL, 0.53 mmol, 8 equiv.) and triphosgene (0.013 g, 0.044 mmol, 0.67 equiv.) were added, and the reaction mixture was stirred at room temperature for 2 h. Subsequently, 4-hexylaniline (0.029 g, 0.165 mmol, 2.5 equiv.) was added, and stirring was continued at room temperature for an additional 12 h. After completion of the reaction, the solvent was removed under reduced pressure, and the crude product was purified by column chromatography (silica gel, CH_2Cl_2/ethyl acetate, 98:2 v/v). The solvent was evaporated, and precipitation was induced using CH_2Cl_2/hexane (3:1 v/v). The resulting solid was filtered and washed with pentane. The product was dried under vacuum to afford a purple solid (0.060 g, 0.051 mmol, and 77%). ^{1}H NMR (DMSO-d_6, 400 MHz): δ (ppm) 8.83 (d, J = 4 Hz, 4H), 8.79 (d, J = 4.8 Hz, 4H), 8.40–8.31 (m, 10H), 7.98 (dd, J_1 = 7.6 Hz, J_2 = 1.6 Hz, 2H), 7.91 (s, 2H), 7.84 (td, J_1 = 8.4 Hz, J_2 = 1.6 Hz, 2H), 7.49 (td, J_1 = 7.6 Hz, J_2 = 0.8 Hz, 2H), 7.20 (s, 2H), 6.74 (s, 8H), 4.04 (s, 6H), 2.29 (t, J = 7.2 Hz, 4H), 1.35 (m, 4H), 1.12 (m, 12H), 0.77 (m, 6H), −2.74 (s, 2H). ^{13}C NMR (DMSO-d_6, 125 MHz): δ (ppm) 166.8, 152.8, 146.2, 140.0, 137.2, 135.9, 135.0, 131.9, 129.8, 129.7, 128.6, 128.3, 122.2, 122.1, 118.0, 116.3, 52.9, 34.7, 31.4, 31.3, 28.6, 22.4, 14.3. MS (MALDI-TOF): m/z calculated for $C_{74}H_{70}N_8O_6$: 1166.54 $[M]^+$ found: 1166.38.

4.6.8 | *Synthesis of Fe–Ur(2)P*

A solution of Ur(2)P (0.045 g, 0.039 mmol, 1 equiv.) and 2,6-lutidine (90 µL, 0.77 mmol, 20 equiv.) 6 mL of dry THF was degassed by nitrogen bubbling for 15 min. Then, $FeBr_2$ (0.083 g, 0.39 mmol, 10 equiv.) was added, and the reaction mixture was stirred overnight at room temperature under nitrogen. The solvent was evaporated under reduced pressure. The solid was dissolved in 25 mL of CH_2Cl_2 and washed with a 25 mL aqueous solution of 1 M HCl. The organic phase was collected and evaporated under reduced pressure. The crude product was purified by column chromatography (silica gel, CH_2Cl_2 to CH_2Cl_2/MeOH, 96:4 v/v), yielding the iron porphyrin complex as a brown solid (0.032 g, 0.025 mmol, 64%). MS (MALDI-TOF): m/z calculated for $C_{74}H_{68}F_{12}FeN_8O_6$: 1220.46, $[M–Cl^-]^+$ found: 1219.49.

1864564x, 2026, 19, Downloaded from https://chemistry-europe.onlinelibrary.wiley.com/doi/10.1002/cssc.71128 by Cochrane Greece, Wiley Online Library on [13/10/2026]. See the Terms and Conditions (https://onlinelibrary.wiley.com/terms-and-conditions) on Wiley Online Library for rules of use; OA articles are governed by the applicable Creative Commons License

4.6.9 | *Synthesis of CAT(2)*

In a 100 mL round-bottom flask, 1 equiv. of Fe–Ur(2)P (0.032 g, 0.025 mmol) was dissolved in 36 mL of a THF/MeOH mixture (2:1). Subsequently, 12 mL of an aqueous 0.36 M KOH solution was added, and the reaction mixture was stirred at room temperature for 48 h. Subsequently, the organic solvents were evaporated under reduced pressure, and distilled water was added to the residue. Acidification of the mixture using an aqueous solution of 1 M HCl resulted in the precipitation of the porphyrin, which was filtered, washed with distilled water, and finally dried under vacuum, yielding the final product as a brown solid (0.065 g, 0.048 mmol, 94%). UV–vis (MeOH) λ_{max} nm (ε, mM^{-1} cm^{-1}) = 340 (24.8), 416 (75.6), 470 (13.5), 601 (3.2), and 645 (2.4). MS (MALDI-TOF): *m/z* calculated for $C_{72}H_{64}FeN_8O_6$: 1192.43, $[M-Cl^-]^+$ found: 1192.28.

4.7 | Chemisorption of Porphyrins Onto TiO_2 NPs

A specific amount of each iron porphyrin (**CAT(1)** and **CAT(2)**) was dissolved in 5 mL of a toluene/ethanol (1:1) solution. After recording the UV–vis absorption spectra of the solutions, 100 mg of TiO_2 was added to each sample. The mixtures were sonicated for 5 min and then stirred for 2 h. After completion of the chemisorption process, the suspensions were filtered, and UV–vis spectra of the filtrates were recorded to determine the chemisorption percentage of each iron porphyrin on TiO_2. The resulting iron porphyrin–TiO_2 nanocomposites were then added to 5 mL of a ZnP solution in chloroform, for which a UV–vis absorption spectrum had been previously obtained. The mixtures were stirred for 1 h at room temperature, followed by filtration. The UV–vis absorption spectra of the filtrates were recorded to evaluate the chemisorption percentage of ZnP on the material. Finally, the samples were dried under vacuum to remove any residual solvent. The concentrations of the iron porphyrin solutions in toluene/ethanol (1:1, 5 mL) used for adsorption were 340 and 32 μM, and the concentrations of the ZnP solutions in chloroform (5 mL) were 600 and 560 μM.

4.8 | Photocatalytic Measurements

The solar-driven CO_2 reduction studies were performed in glass vials (41.9 mL), sealed with a rubber septum, at ambient temperature and pressure. Before each experiment, a fresh acetonitrile solution, which contained the SED, was prepared. The dyed TiO_2 NPs (10 mg) were added to the glass vial together with 4 mL of the abovementioned solution. The samples were sealed with a silicon septum and then bubbled for 5 min with CO_2. Finally, the samples were irradiated under continuous stirring with a low-power white LED lamp ring with a color temperature of 6400 K and a lumen of 3800 LM. This setup provided defined positions and a certain amount ($50\,W \cdot cm^{-2}$) of the emitted light for all the vials simultaneously. The amount of CO and H_2 production of each sample vial was determined using a Shimadzu GC 2010 plus chromatograph with a TCD detector and a molecular sieve 5 Å column (30 m–0.53 mm). For every measurement, 100 μL was taken from the headspace of the vial and was instantly injected in the GC. In all cases, both the reported CO and H_2 values, as well as the TON, are the average of three independent experiments. The reaction solution was additionally analyzed for formate by ion-exchange chromatography, and no formate was detected under the conditions employed herein. Formate selectivity in related iron-porphyrin systems requires a strong organic base to tune the reaction pKa [59, 60], which is absent from the present reaction medium. TON and selectivity are therefore reported with respect to CO and H_2, the only products detected.

4.9 | Calculation of TON

The TONs were calculated according to the following equation:

$$\mathbf{TON} = \frac{\boldsymbol{n}(\mathbf{CO})}{\boldsymbol{n}(\mathbf{CAT})}$$

where $\boldsymbol{n}$**(CO)** is the total amount of **CO** produced and $\boldsymbol{n}$**(CAT)** is the total amount of catalyst adsorbed on the TiO_2 surface.

Acknowledgments

This research has been financed by the European Union's Horizon Europe research and innovation programme under Grant Agreement No. 101120397 (project: APPROACH). Moreover, Emmanouil Nikoloudakis gratefully acknowledges the Bodossaki Foundation for the financial support. This work was partially supported by the "Hubert Curien 2023 Partnership" programme (DISPHORED).

The publication of this article in OA mode was financially supported by HEAL-Link.

Funding

This study was supported by the European Union's Horizon Europe research and innovation programme (101120397), and Bodossaki Foundation.

Conflicts of Interest

The authors declare no conflicts of interest.

Data Availability Statement

The data that support the findings of this study are available in the Supporting Information of this article.

References

1. L. J. R. Nunes, "The Rising Threat of Atmospheric CO_2: A Review on the Causes, Impacts, and Mitigation Strategies," *Environments* 10 (2023): 66, https://doi.org/10.3390/environments10040066.

2. V. Kumaravel, J. Bartlett, and S. C. Pillai, "Photoelectrochemical Conversion of Carbon Dioxide (CO_2) into Fuels and Value-Added Products," *ACS Energy Letters* 5 (2020): 486, https://doi.org/10.1021/acsenergylett.9b02585.

3. W. Hou, W. H. Hung, P. Pavaskar, A. Goeppert, M. Aykol, and S. B. Cronin, "Photocatalytic Conversion of CO_2 to Hydrocarbon Fuels via Plasmon-Enhanced Absorption and Metallic Interband Transitions," *ACS Catalysis* 1 (2011): 929, https://doi.org/10.1021/cs2001434.

4. J. Bonin, M. Robert, and M. Routier, "Selective and Efficient Photocatalytic CO_2 Reduction to CO Using Visible Light and an Iron-Based Homogeneous Catalyst," *Journal of the American Chemical Society* 136 (2014): 16768, https://doi.org/10.1021/ja510290t.

1864564x, 2026, 19, Downloaded from https://chemistry-europe.onlinelibrary.wiley.com/doi/10.1002/cssc.71128 by Cochrane Greece, Wiley Online Library on [13/10/2026]. See the Terms and Conditions (https://onlinelibrary.wiley.com/terms-and-conditions) on Wiley Online Library for rules of use; OA articles are governed by the applicable Creative Commons License

5. S. Gu, A. N. Marianov, T. Lu, and J. Zhong, "A Review of the Development of Porphyrin-Based Catalysts for Electrochemical CO_2 Reduction," *Chemical Engineering Journal* 9 (2019): 144249.

6. A. Call, M. Cibian, K. Yamamoto, T. Nakazono, K. Yamauchi, and K. Sakai, "Highly Efficient and Selective Photocatalytic CO_2 Reduction to CO in Water by a Cobalt Porphyrin Molecular Catalyst," *ACS Catalysis* 9 (2019): 4867, https://doi.org/10.1021/acscatal.8b04975.

7. X. Zhang, K. Yamauchi, and K. Sakai, "Earth-Abundant Photocatalytic CO_2 Reduction by Multielectron Chargeable Cobalt Porphyrin Catalysts: High CO/H_2 Selectivity in Water Based on Phase Mismatch in Frontier MO Association," *ACS Catalysis* 11 (2021): 10436, https://doi.org/10.1021/acscatal.1c02475.

8. H. Kumagai, Y. Tamaki, and O. Ishitani, "Photocatalytic Systems for CO_2 Reduction: Metal-Complex Photocatalysts and Their Hybrids with Photofunctional Solid Materials," *Accounts of Chemical Research* 55 (2022): 978, https://doi.org/10.1021/acs.accounts.1c00705.

9. Y.-N. Jing, H.-X. Wang, C. Wang, C. Ye, C.-H. Tung, and L.-Z. Wu, "A Highly Efficient Molecular Iron(II) Photocatalyst for Concurrent CO_2 Reduction and Organic Synthesis," *Journal of the American Chemical Society* 147 (2025): 15942, https://doi.org/10.1021/jacs.5c01698.

10. P. Ncube and M. J. Mochane, "Visible-Light-Driven CO_2 Photoreduction Using Ruthenium (II) Complexes: Mechanisms, Hybrid Systems and Recent Advances," *Catalysts* 20 (2024): 1036.

11. Z. Yuan, X. Zhu, X. Gao, et al., "Enhancing Photocatalytic CO_2 Reduction with TiO_2-Based Materials: Strategies, Mechanisms, Challenges, and Perspectives," *Environmental Science and Ecotechnology* 20 (2024): 100368, https://doi.org/10.1016/j.ese.2023.100368.

12. Žan Kovačič, Ž Likozar, and M. Huš, "Photocatalytic CO_2 Reduction: A Review of Ab Initio Mechanism, Kinetics, and Multiscale Modeling Simulations," *ACS Catalysis* 10 (2020): 14984, https://doi.org/10.1021/acscatal.0c02557.

13. J. Willkomm, K. L. Orchard, A. Reynal, E. Pastor, J. R. Durrant, and E. Reisner, "Dye-Sensitised Semiconductors Modified with Molecular Catalysts for Light-Driven H_2 Production," *Chemical Society Reviews* 45 (2016): 9, https://doi.org/10.1039/C5CS00733J.

14. S. Xu, X. Li, S. Li, et al., "Recent Advances of Photocatalytic CO_2 Reduction Based on Hybrid Molecular Catalyst/Semiconductor Photocatalysts: A Review," *Small* 21 (2025): 2408075, https://doi.org/10.1002/smll.v21.4.

15. V. Nikolaou, C. Govind, E. Balanikas, et al., "Antenna Effect in Noble Metal-Free Dye-Sensitized Photocatalytic Systems Enhances CO_2-to-CO Conversion," *Angewandte Chemie International Edition* 63 (2024): e202318299, https://doi.org/10.1002/anie.v63.13.

16. V. Nikolaou, E. Nikoloudakis, G. Charalambidis, and A. G. Coutsolelos, "Dye-Sensitized Nanoparticles for Efficient Solar Hydrogen Generation," *Chemical Communications* 61 (2025): 10086, https://doi.org/10.1039/D5CC01971K.

17. A. W. Nichols and C. W. Machan, "Secondary-Sphere Effects in Molecular Electrocatalytic CO_2 Reduction," *Frontiers in Chemistry* 7 (201913592, https://doi.org/10.3389/fchem.2019.00397.

18. S. Amanullah, P. Saha, and A. Dey, "Activating the Fe(I) State of Iron Porphyrinoid with Second-Sphere Proton Transfer Residues for Selective Reduction of CO_2 to HCOOH via Fe(III/II)–COOH Intermediate(s)," *Journal of the American Chemical Society* 143 (2021): 13579, https://doi.org/10.1021/jacs.1c04392.

19. P. Saha, S. Amanullah, and A. Dey, "Selectivity in Electrochemical CO_2 Reduction," *Accounts of Chemical Research* 55 (2022): 134, https://doi.org/10.1021/acs.accounts.1c00678.

20. S. Amanullah, P. Saha, A. Nayek, M. E. Ahmed, and A. Dey, "Biochemical and Artificial Pathways for the Reduction of Carbon Dioxide, Nitrite and the Competing Proton Reduction: Effect of 2nd Sphere Interactions in Catalysis," *Chemical Society Reviews* 50 (2021): 3755, https://doi.org/10.1039/D0CS01405B.

21. S. Sinha, C. K. Williams, and J. J. Jiang, "Outer-Coordination Sphere in Multi-H+/Multi-e–Molecular Electrocatalysis," *iScience* 25(2022): 103628.

22. S. Amanullah, P. Gotico, M. Sircoglou, et al., "Second Coordination Sphere Effect Shifts CO_2 to CO Reduction by Iron Porphyrin from Fe^0 to Fe^I," *Angewandte Chemie International Edition* 63 (2024): e202314439, https://doi.org/10.1002/anie.v63.4.

23. P. Gotico, B. Boitrel, R. Guillot, et al., "Second-Sphere Biomimetic Multipoint Hydrogen-Bonding Patterns to Boost CO_2 Reduction of Iron Porphyrins," *Angewandte Chemie International Edition* 58 (2019): 4504, https://doi.org/10.1002/anie.v58.14.

24. E. Pugliese, P. Gotico, I. Wehrung, et al., "Dissection of Light-Induced Charge Accumulation at a Highly Active Iron Porphyrin: Insights in the Photocatalytic CO_2 Reduction," *Angewandte Chemie International Edition* 61 (2022): e202117530, https://doi.org/10.1002/anie.v61.14.

25. S. Fang, M. Rahaman, J. Bharti, et al., "Photocatalytic CO_2 Reduction," *Nature Reviews Methods Primers* 3 (2023): 61, https://doi.org/10.1038/s43586-023-00243-w.

26. D.-I. Won, J.-S. Lee, Q. Ba, et al., "Development of a Lower Energy Photosensitizer for Photocatalytic CO_2 Reduction: Modification of Porphyrin Dye in Hybrid Catalyst System," *ACS Catalysis* 8 (2018): 1018, https://doi.org/10.1021/acscatal.7b02961.

27. E. Nikoloudakis, I. López-Duarte, G. Charalambidis, K. Ladomenou, M. Ince, and A. G. Coutsolelos, "Porphyrins and Phthalocyanines as Biomimetic Tools for Photocatalytic H_2 Production and CO_2 Reduction," *Chemical Society Reviews* 51 (2022): 6965, https://doi.org/10.1039/D2CS00183G.

28. K. Sun, Y. Qian, and H.-L. Jiang, "Metal-Organic Frameworks for Photocatalytic Water Splitting and CO_2 Reduction," *Angewandte Chemie International Edition* 62 (2023): e202217565, https://doi.org/10.1002/anie.v62.15.

29. D. Saito, Y. Tamaki, and O. Ishitani, "Photocatalysis of CO_2 Reduction by a Ru(II)–Ru(II) Supramolecular Catalyst Adsorbed on Al_2O_3," *ACS Catalysis* 13 (2023): 4376, https://doi.org/10.1021/acscatal.2c06247.

30. C.-W. Lee, H.-P. Lu, C.-M.Lan, et al., "Novel Zinc Porphyrin Sensitizers for Dye-Sensitized Solar Cells: Synthesis and Spectral, Electrochemical, and Photovoltaic Properties," *Chemistry – A European Journal* 15 (2009): 1403, https://doi.org/10.1002/chem.v15:6.

31. W. M. Campbell, A. K. Burrell, D. L. Officer, and K. W. Jolley, "Porphyrins as Light Harvesters in the Dye-Sensitised TiO_2 Solar Cell," *Coordination Chemistry Reviews* 248 (2004): 1363, https://doi.org/10.1016/j.ccr.2004.01.007.

32. S. Karthikeyan and J. Y. Lee, "Zinc-Porphyrin Based Dyes for Dye-Sensitized Solar Cells," *Journal of Physical Chemistry A* 117 (2013): 10973, https://doi.org/10.1021/jp408473k.

33. S. Ye, A. Kathiravan, H. Hayashi, et al., "Role of Adsorption Structures of Zn-Porphyrin on TiO_2 in Dye-Sensitized Solar Cells Studied by Sum Frequency Generation Vibrational Spectroscopy and Ultrafast Spectroscopy," *Journal of Physical Chemistry C* 117 (2013): 6066, https://doi.org/10.1021/jp400336r.

34. V. Nikolaou, C. Govind, E. Balanikas, et al., "Antenna Effect in Noble Metal-Free Dye-Sensitized Photocatalytic Systems Enhances CO_2 -to-CO Conversion," *Angewandte Chemie* 136 (2024): e202318299, https://doi.org/10.1002/ange.v136.13.

35. S. Choi, M. S. Choe, D. Lee, et al., "Efficient Photosensitization of π-Extended Oligomeric Porphyrin Pigments through TiO_2 -Mediated Outer-Sphere Electron Transfer in Photochemical CO_2 Reduction Systems," *ACS Applied Energy Materials* 7 (2024): 3602, https://doi.org/10.1021/acsaem.3c03048.

36. E. Nikoloudakis, P. B. Pati, G. Charalambidis, et al., "Dye-Sensitized Photoelectrosynthesis Cells for Benzyl Alcohol Oxidation Using a Zinc

1864564x, 2026, 19, Downloaded from https://chemistry-europe.onlinelibrary.wiley.com/doi/10.1002/cssc.71128 by Cochrane Greece, Wiley Online Library on [13/10/2026]. See the Terms and Conditions (https://onlinelibrary.wiley.com/terms-and-conditions) on Wiley Online Library for rules of use; OA articles are governed by the applicable Creative Commons License

Porphyrin Sensitizer and TEMPO Catalyst," *ACS Catalysis* 11 (2021): 12075, https://doi.org/10.1021/acscatal.1c02609.

37. P.-Y. Ho, M. F. Mark, Y. Wang, et al., "Panchromatic Sensitization with Zn^{II} Porphyrin-Based Photosensitizers for Light-Driven Hydrogen Production," *ChemSusChem* 11 (2018): 2517, https://doi.org/10.1002/cssc.v11.15.

38. Y. Kuramochi, Y. Fujisawa, and A. Satake, "Photocatalytic CO_2 Reduction Mediated by Electron Transfer via the Excited Triplet State of Zn(II) Porphyrin," *Journal of the American Chemical Society* 142 (2020): 705, https://doi.org/10.1021/jacs.9b12712.

39. H. Kang, D. Lee, S. Jeong, et al., "Efficient and Durable Photochemical CO_2 Reduction by TiO_2 -Immobilized Metal Porphyrin Catalysts," *ChemSusChem* 19 (2026): e202501889, https://doi.org/10.1002/cssc.v19.7.

40. Y. Pellegrin and F. Odobel, "Sacrificial Electron Donor Reagents for Solar Fuel Production," *Comptes Rendus Chimie* 20(2017):283.

41. A. S. Rury and R. J. Sension, "Broadband Ultrafast Transient Absorption of Iron(III) Tetraphenylporphyrin Chloride in the Condensed Phase," *Chemical Physics* 422 (2013): 220, https://doi.org/10.1016/j.chemphys.2013.01.025.

42. M. Taniguchi, J. S. Lindsey, D. F. Bocian, and D. Holten, "Comprehensive Review of Photophysical Parameters (ε, Φ_f, τ_s) of Tetraphenylporphyrin (H2TPP) and Zinc Tetraphenylporphyrin (ZnTPP) – Critical Benchmark Molecules in Photochemistry and Photosynthesis," *Journal of Photochemistry and Photobiology C: Photochemistry Reviews* 46 (2021): 100401, https://doi.org/10.1016/j.jphotochemrev.2020.100401.

43. L. A. Constant and D. G. Davis, "Electrochemical Characterization of Iron Porphyrin Complexes in Aprotic Solvents," *Analytical Chemistry* 47 (1975): 2253, https://doi.org/10.1021/ac60363a051.

44. P.-A. Faugeras, B. Boëns, P.-H. Elchinger, J. Vergnaud, K. Teste, and R. Zerrouki, "Synthesis of Meso-Substituted Dipyrromethanes Using Iodine-Catalysis," *Tetrahedron Letters* 51 (2010): 4630, https://doi.org/10.1016/j.tetlet.2010.06.122.

45. K. Heinze and A. Reinhart, "A New Hydrogen-Bonding Motif with Constituents Bearing Donor and Acceptor Sites 7 A Apart," *Zeitschrift für Naturforschung B* 60 (2005): 758.

46. T. Rohand, E. Dolusic, T. H. Ngo, W. Maes, W. Dehaen, and G. Cirrincione, "Efficient Synthesis of Aryldipyrromethanes in Water and Their Application in the Synthesis of Corroles and Dipyrromethenes," *Arkivoc* 2007 (2007): 307, https://doi.org/10.3998/ark.5550190.0008.a20.

47. D. M. Wallace, S. H. Leung, M. O. Senge, and K. M. Smith, "Rational Tetraarylporphyrin Syntheses: Tetraarylporphyrins from the MacDonald Route," *Journal of Organic Chemistry* 58 (1993): 7245, https://doi.org/10.1021/jo00077a056.

48. C. Römelt, S. Ye, E. Bill, T. Weyhermüller, M. van Gastel, and F. Neese, "Electronic Structure and Spin Multiplicity of Iron Tetraphenylporphyrins in Their Reduced States as Determined by a Combination of Resonance Raman Spectroscopy and Quantum Chemistry," *Inorganic Chemistry* 57 (2018): 2141, https://doi.org/10.1021/acs.inorgchem.7b03018.

49. G. Deacon, "Relationships between the Carbon-Oxygen Stretching Frequencies of Carboxylato Complexes and the Type of Carboxylate Coordination," *Coordination Chemistry Reviews* 33 (1980): 227, https://doi.org/10.1016/S0010-8545(00)80455-5.

50. D. Wechsler, P. Vensaus, N. Tsud, H.-P. Steinrück, O. Lytken, and F. J. Williams, "Surface Reactions and Electronic Structure of Carboxylic Acid Porphyrins Adsorbed on TiO_2 (110)," *Journal of Physical Chemistry C* 125 (2021): 6708, https://doi.org/10.1021/acs.jpcc.1c01133.

51. B. Vaz and M. Pérez-Lorenzo, "Unraveling Structure–Performance Relationships in Porphyrin-Sensitized TiO_2 Photocatalysts," *Nanomaterials* 13 (2023): 1097, https://doi.org/10.3390/nano13061097.

52. C. D. Windle, E. Pastor, A. Reynal, et al., "Improving the Photocatalytic Reduction of CO_2 to CO through Immobilisation of a Molecular Re Catalyst on TiO_2," *Chemistry – A European Journal* 21 (2015): 3746, https://doi.org/10.1002/chem.v21.9.

53. L. Zani, M. Melchionna, T. Montini, and P. Fornasiero, "Design of Dye-Sensitized TiO_2 Materials for Photocatalytic Hydrogen Production: Light and Shadow," *Journal of Physics: Energy* 3 (2021): 031001, https://doi.org/10.1088/2515-7655/abe04b.

54. K. Kamogawa, H. Koizumi, and O. Ishitani, "Efficient and Selective Photocatalytic Conversion of Low-Concentration CO_2 to CO Using Mn-Complex Catalysts," *Journal of the American Chemical Society* 147 (2025): 39284, https://doi.org/10.1021/jacs.5c10694.

55. J. J. Warren, A. R. Menzeleev, J. S. Kretchmer, T. F. Miller III, H. B. Gray, and J. M. Mayer, "Long-Range Proton-Coupled Electron-Transfer Reactions of Bis(imidazole) Iron Tetraphenylporphyrins Linked to Benzoates," *Journal of Physical Chemistry Letters* 4 (2013): 519, https://doi.org/10.1021/jz400029w.

56. J.-Y. Chen, M. Li, and R.-Z. Liao, "Mechanistic Insights into Photochemical CO_2 Reduction to CH_4 by a Molecular Iron–Porphyrin Catalyst," *Inorganic Chemistry* 62 (2023): 9400, https://doi.org/10.1021/acs.inorgchem.3c00402.

57. W. Sun, Z. Li, X. Meng, N. Li, X. Liang, and Y. Ding, "Recent Advances and Perspectives on Porphyrin for Photocatalytic CO_2 Reduction: From Molecules to Framework Materials," *Chemical Record* 25 (2025): e202500101.

58. M. Imai, S. Masaoka, and M. Kondo, "Function Provision to Fe–Porphyrin Complexes for CO_2 Reduction," *JACS Au* 5(2025):3716.

59. X. Yao, W.-J. Xie, L. Qiu, and L.-N. He, "Organic Bases-Mediated CO_2 Photoreduction Coupled with N-Heterocycle Dehydrogenation," *ChemSusChem* 18 (2025): e202501750, https://doi.org/10.1002/cssc.v18.24.

60. X. Yao, L. Qiu, W.-J. Xie, and L.-N. He, "Switchable CO_2 Photoreduction Selectivity via Organic Bases in Dual-Component Earth-Abundant Metal Systems," *ACS Sustainable Chemistry & Engineering* 13 (2025): 10223, https://doi.org/10.1021/acssuschemeng.5c04189.

Supporting Information

Additional supporting information can be found online in the Supporting Information section.

1864564x, 2026, 19, Downloaded from https://chemistry-europe.onlinelibrary.wiley.com/doi/10.1002/cssc.71128 by Cochrane Greece, Wiley Online Library on [13/10/2026]. See the Terms and Conditions (https://onlinelibrary.wiley.com/terms-and-conditions) on Wiley Online Library for rules of use; OA articles are governed by the applicable Creative Commons License